PHYSICAL REVIEW B **105**, 195410 (2022)

Electrically tunable magnetism and unique intralayer charge transfer in Janus monolayer MnSSe for spintronics applications

Yu Chen,[1] Qiang Fan,[2] Yiding Liu,[3] and Gang Yao[4,*]
[1] *School of Science, Inner Mongolia University of Technology, Hohhot 010051, China*
[2] *School of New Energy Materials and Chemistry, Leshan Normal University, Leshan 614004, China*
[3] *College of Mathematics and Physics, Leshan Normal University, Leshan 614004, China*
[4] *Tsung-Dao Lee Institute, Shanghai Jiao Tong University, Shanghai 200240, China*

(Received 3 October 2021; accepted 26 April 2022; published 6 May 2022)

Controlling magnetism and electronic properties of two-dimensional (2D) materials by purely electrical means is crucial and highly sought for high-efficiency spintronics devices since electric field can be easily applied locally compared with magnetic field. The recently discovered 2D Janus crystals provide a platform for nanoscale electronics and spintronics due to their broken inversion symmetry. Here, through comprehensive density functional theory calculations and Monte Carlo simulations, we demonstrate that both the electronic and magnetic properties of Janus monolayer MnSSe, a 2D ferromagnetic half-metal with high Curie temperature, are electrically tunable. The exchange coupling can be significantly enhanced or quenched by hole and electron doping, respectively. In particular, with a small amount of hole doping, MnSSe can tune its magnetization easy axis in between out-of-plane and in-plane directions, which is conducive to designing a 2D spin field effect transistor for spin-dependent transport. We also find a reversible longitudinal intralayer charge transfer between S and Se layers that is highly sensitive to the external electric field. Interestingly, the directions of charge flow and the applied field are the same. This behavior originates from the coexistence and/or the competition of external and built-in electric fields. These findings, together with the excellent stability and large in-plane stiffness, can greatly facilitate the development of nanoscale electronics and spintronics devices based on 2D MnSSe crystal.

DOI: 10.1103/PhysRevB.105.195410

I. INTRODUCTION

Spintronics or spin-based electronics devices formed based on spin and charge degrees of freedom of electrons have long held promise for developing high-efficiency information technology and fundamental physics [1,2]. During the last decade, plenty of two-dimensional (2D) materials were discovered and proposed. Among all these systems, transition metal dichalcogenides (TMDCs) are some of the most typical representative because some of them host unique electronic and optical properties compared to the star material, graphene [3,4]. Although TMDCs host intrinsic in-plane asymmetry, the out-of-plane mirror symmetry is considered a disadvantage that limits the spin degrees of freedom and therefore hinders their wide applications in valleytronics, spintronics, and magneto-optoelectronics. Experimentally, by applying an external electric field out-of-plane inversion asymmetry in 2D nanosheets was successfully achieved [5,6]. Alternatively, broken inversion symmetry was also proposed in stable TMDC monolayer with a distinct two surfaces, a system now known as Janus TMDCs [7]. The successful synthesis of single-layer MoSSe by chemical vapor deposition brought forward in recent years made the research on Janus crystals reach a climax [8,9]. The potential applications of Janus materials and their superlattices in different areas, such as sodium-ion batteries, ultrafast laser, photocatalysts, electronics, energy conversion, sensor, and quantum sciences, have been extensively analyzed [10–13].

With respect to spintronic applications, intrinsic ferromagnetic half-metal with a high Curie temperature property and its precise and flexible controllability are highly desirable. We note that some of the single-layer Janus TMDCs have been recently predicated to be intrinsic ferromagnets, including MnSSe, which was claimed to be a ferromagnetic half-metal with a Curie temperature of 185 K [14]. These results provide value perspective on this system. But the structure stability, and magnetocrystalline anisotropy that determines the low-temperature character of the ferromagnetic ordering of a magnetic 2D material, were not well explored. Also, the possibility to precisely control ferromagnetic stability in this system remains unknown. For instance, it is demonstrated that carrier doping and electric field can efficiently modulate the performance of 2D crystals [15–20]. Electrically controllable magnetic anisotropy is critical to nonvolatile magnetoelectric random access memory [21]. Such an investigation in Janus monolayer, however, has rarely been reported in the literature. On the other hand, the out-of-plane asymmetric will inevitably produce a built-in electronic field; one central issue that naturally arises is how the charges will behave in this nontrivial sandwichlike structure under external electric fields. The above questions deserve a careful investigation. This phenomenon will promote the development of spintronics or spin-based electronics.

In this paper, we perform DFT calculations to explore the electronic control of ferromagnetism and intralayer charger

---

[*] Corresponding author: yaogang1257@sjtu.edu.cn

transfer in 2D MnSSe crystal. We show that the ferromagnetic half-metallic $1T$ structure is lower in energy than the $2H$ structure and possesses relatively high in-plane stiffness. Calculations of magnetocrystalline anisotropy energy (MAE) shows an out-of-plane spin orientation, which reinforces the proposal of long-range ferromagnetism order in this material. Under this prerequisite, we demonstrate that the magnetic coupling can be considerably enhanced or quenched with carrier doping. Intriguingly, the magnetization can be changed from an easy plane to an easy axis with a small amount of hole doping, allowing for the realization of spin field effect transistor (spin-FET), as we shown in this work. Further, a unique intralayer charge transfer behavior with respect to the direction of applied external electric field is presented and explained based on the unusual crystal structure.

II. COMPUTATIONAL DETAILS

Our calculations are performed using a plane-wave basis set and projector augmented-wave method [22,23] as implemented in the Vienna Ab initio Simulation Package (VASP) code [24]. The GGA-PBE exchange-correlation functionals [25] are used to describe the electron-ion interactions. The kinetic cutoff energy is set to 420 eV. To avoid the interlayer interactions, a vacuum spacing of 15 Å is introduced in the direction normal to the sheet. The convergence criterion for energy is 1×10^{-6} eV. The $3p^6 4s^2 3d^5$, $3s^2 3p^4$, and $4s^2 4p^4$ states are treated as valence states for Mn, S, and Se atoms, respectively. We use the GGA + U_{eff} method introduced by Dudarev *et al.* [26] to describe the localized Mn-3d orbital. According to previous reports [14,27], $U_{\text{eff}} = U - J = 3$ is selected, where U and J denote on-site Coulomb and exchange parameters and are set to 3.7 and 0.7 eV, respectively. For noncollinear calculations, the spin-orbit coupling (SOC) interaction is considered and performed on a unit cell. The Brillouin zone integration is performed using Γ-centered k-point meshes of $11 \times 11 \times 1$ and $23 \times 23 \times 1$ for a primitive unit cell, and $2 \times 2 \times 1$ supercell, respectively. Test calculations with large energy cutoff and k-point mesh demonstrated that the results are fully converged. The dipole corrections perpendicular to the 2D plane were included as a counterpart to the possible built-in electric field introduced by the out-of-plane geometric asymmetry.

Carrier doping is simulated by adding or removing electrons into the system, and a uniform background charge is adopted to maintain charge neutrality. Phonon dispersion is calculated on a $5 \times 5 \times 1$ supercell by the finite displacement method [28] with a displacement of 0.1 Å, as embedded in the PHONOPY code [29]. To explore the magnetic coupling versus temperature Monte Carlo (MC) Metropolis algorithm simulations based on the 2D Ising model are performed. Within the MC scheme, the spins on all magnetic sites flip randomly, and a $100 \times 100 \times 1$ supercell containing ~10 000 local magnetic moments is used to reduce the periodic constraints. At each temperature, the equilibrated magnetic moment is taken after the simulations lasted for 1×10^7 loops. The crystal structure and charge density are visualized by VESTA software [30]. The VASPKIT program [31] is employed in both the pre- and postdata processing.

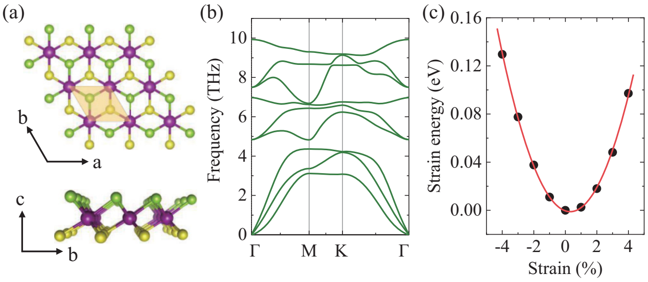

FIG. 1. (a) Top and side view of a MnSSe monolayer with $1T$ phase, where Mn, S, and Se atoms are purple, yellow, and green, respectively. The orange shaded region indicates the primitive unit cell. (b) Calculated phonon dispersion for 2D MnSSe crystal. (c) The strain energy of MnSSe monolayer under uniaxial strain.

III. RESULTS AND DISCUSSION

A. Stability of single-layer MnSSe

Janus TMDC monolayers are isostructural to the TMDCs, and generally exist in trigonal and octahedral prismatic coordination in $1T$ and $2H$ phases. Our calculation shows that the $1T$ structure is 400 meV lower in energy than the $2H$ one in MnSSe. We henceforth only focus on the $1T$ structure [Fig. 1(a)].

To check the chemical stability, we calculated the cohesive energy by $E_{\text{coh}} = (E_{\text{Mn}} + E_{\text{S}} + E_{\text{Se}} - E_{\text{MnSSe}})/3$, where E_{MnSSe}, E_{Mn}, E_{S}, and E_{Se} are the energy of 2D MnSSe unit cell and free atoms of Mn, S, and Se, respectively. The obtained $E_{\text{cho}} = 3.83\,\text{eV/atom}$ is very close to silicene (3.98 eV/atom) [32] and germane (3.26 eV/atom) [32]. The formation energy (E_{f}) of 2D MnSSe from the competing stable bulk compounds, MnS_2 and $MnSe_2$, can be estimated by $E_{\text{f}} = (2E_{\text{MnSSe}}\text{-}E_{\text{MnS}}\text{-}E_{\text{MnSe}})/3$, where E_{MnS2} and E_{MnSe2} are the energy of one formula unit of stoichiometric bulk MnS_2 and bulk $MnSe_2$, respectively. The calculated $E_{\text{f}} = 114\,\text{meV/atom}$ is sufficiently low, implying that there is a chance to synthesize this material. Figure 1(b) displays the calculated phonon dispersion, in which no imaginary-vibration mode was found at the discretionary wave vector, indicating the dynamical stability of single-layer MnSSe. Thus, 2D MnSSe crystal with $1T$ structure can be considered stable.

For the fabrication of low-dimensional crystal-based electronics or spintronics devices, high in-plane stiffness is crucial to avoiding the curling or bulking of a 2D nanosheet. In-plane stiffness can be estimated by the 2D Young's modulus:

$$Y_{2\text{D}} = \frac{1}{S_0}\left(\frac{\partial^2 E_s}{\partial \varepsilon^2}\right)_{\varepsilon=0}, \tag{1}$$

$$\varepsilon = (l - l_0)/l_0, \tag{2}$$

where the strain energy E_{s} is the energy difference with reference to pristine MnSSe layer and ε denotes the in-plane uniaxial strain. l and l_0 denote the strained and unstrained lattice constants, respectively. S_0 is the unstrained surface area. Based on the optimized lattice constant 3.522 Å, we plotted E_s versus ε in the range −4–4% in Fig. 1(c). $Y_{2\text{D}}$ is estimated to be 53 N/m, which is very close to the predicated values of $MnPSe_3$ (36 N/m) [33], $CrGeTe_3$ (38.3 N/m) [34], Nb_3X_8 (X = Cl, Br, and I) (46–65 N/m) [35], and monolayer

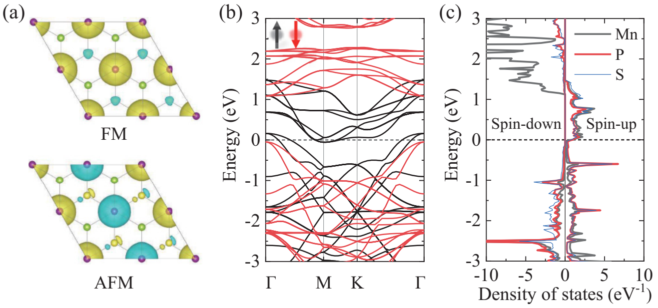

FIG. 2. (a) Spin-resolved charge density with an isovalue of $0.015\,\mathrm{e}/\text{Å}^3$ in the FM and AFM states. Yellow (blue) ones indicate the positive (negative) values. (b) Spin-resolved electronic band structures. The black (red) line represents the spin-up (spin-down) bands. (c) Projected density of state. In (b) and (c), the Fermi level is denoted by the dotted line at zero.

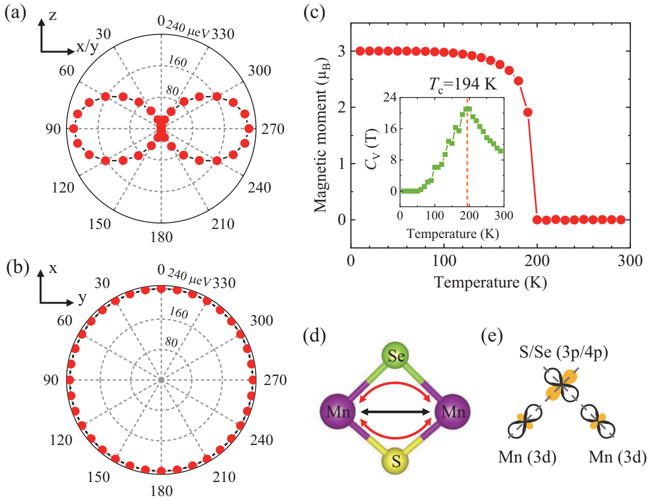

FIG. 3. (a), (b) Dependence of the MAE per Mn atom for pristine single-layer MnSSe on the out-of-plane polar angle θ and in-plane azimuth angle φ, respectively. (c) The simulated magnetic moment and specific heat (C_v) with respect to temperature, showing a T_c of about 194 K. (d) Schematic mechanism of direct Mn-Mn (black arrows) and superexchange Mn-S(Se)-Mn (red arrows) interactions. (e) Mechanism of superexchange interaction for a nearly 90° Mn-S(Se)-Mn bond angle.

FeSe (80 N/m) [36]. Nevertheless, this value extracted here is significantly lower than that of graphene (∼340 N/m) [37], indicating the soft and flexible nature of MnSSe monolayer that would facilitate its application under external strain.

Then, according to the elastic theory, one can derive the gravity-induced out-of-plane deformation h as follows [38]:

$$h/L \approx (\rho g L/Y_{2D})^{1/3}, \tag{3}$$

where $\rho = 2.57 \times 10^{-6}\,\mathrm{kg/m^2}$ is the density of the MnSSe monolayer and g is the gravitational acceleration (9.81 N/kg). For convenient comparison with the previous works [33–35], we take the size of the flake $L = 100\,\mu\mathrm{m}$, resulting in $h/L = 3.63 \times 10^{-4}$, which is comparable to that of graphene [38]. Therefore, monolayer MnSSe hosts sufficient rigidity and can keep the free-standing planar structure without substrate.

B. Intrinsic half-metallic ferromagnetism

Magnetic studies show that ferromagnetic (FM) configuration is the ground state of the single-layer MnSSe [Fig. 2(a)], which is lower in energy than antiferromagnetic (AFM) and nonmagnetic (NM) states by an energy difference of 80 meV and 2.8 eV per unit cell, respectively. The net magnetic moment is $M = 3\mu_B$ per unit cell, implying a large spin polarization in this material. The local magnetic moment of the Mn atom is $M_{Mn} = 3.654\mu_B$, consistent with the high spin state of Mn^{3+}. S and Se atoms carry an extensively small opposite moment ($M_S = -0.223\mu_B$ and $M_{Se} = -0.322\mu_B$); they are antiferromagnetically coupled to Mn atoms and hardly magnetized. Therefore, the spin polarizations are mainly dominated by Mn atoms. The spin-resolved band structure of MnSSe in the FM state is shown in Fig. 2(b). Electrons of the spin-down channel are insulating with a direct band gap of 1.14 eV at the Γ point, while those of the spin-up channel are metallic with a negative gap of −0.2 eV, suggesting the half-metallic nature of MnSSe. These results are consistent with previous reports [14,39]. From the calculated atom projected density of states, the bands near the Fermi level of the two spin channels are contributed jointly by the Mn, S, and Se states [Fig. 2(c)].

MAE determines the type of magnetic order at low temperature; it denotes the energy needed to overcome the "barrier" when moving the direction of a magnetic moment from the easy axis to the hard one. Magnetic 2D materials with easy-plane magnetic anisotropy possess a quasi-long-range ordered phase at low temperature. Meanwhile, Berezinskii-Kosterlitz-Thouless (BKT) transition occurs at crucial temperature with a change of an exponential law spin-spin correlation function behavior above T_{BKT} to a power law one below it. By contrast, 2D crystal with an easy-axis magnetic anisotropy exhibits the so-called Curie transition or ferromagnetic transition to a long-range ordered low-temperature phase, i.e., a ferromagnetically ordered low-temperature phase [40]. MAE can be calculated as MAE $= E_{[uvw]} - E_{\min}$, where $E_{\min}$ denotes the energy of the most stable spin orientation. The polar angle dependence of MAE on the xz, yz, and xy planes is illustrated in Figs. 3(a) and 3(b). we observed a strong dependence of the MAE on the θ, and a negligible dependence on the φ. MAE is 0 at $\theta = 0°$ or 180°, and reaches a maximum value of 220 μeV per Mn atom in the xy plane, implying a preferred out-of-plane axis. Therefore, 1T -MnSSe monolayer belongs to the family of 2D Ising magnets. Above zero temperature, the existence of heat fluctuation can destroy the long-range order; the large MAE found here will help to stabilize this ordering at a higher temperature.

To understand the temperature effect on the magnetism, we then performed the standard Monte Carlo Metropolis algorithm simulations based on the Ising Hamiltonian model,

$$\hat{H} = -\sum_{i,j} J_{ij} M_i M_j, \tag{4}$$

where J_{ij} represents the nearest-neighboring exchange coupling constant, positive for ferromagnetic interaction, and

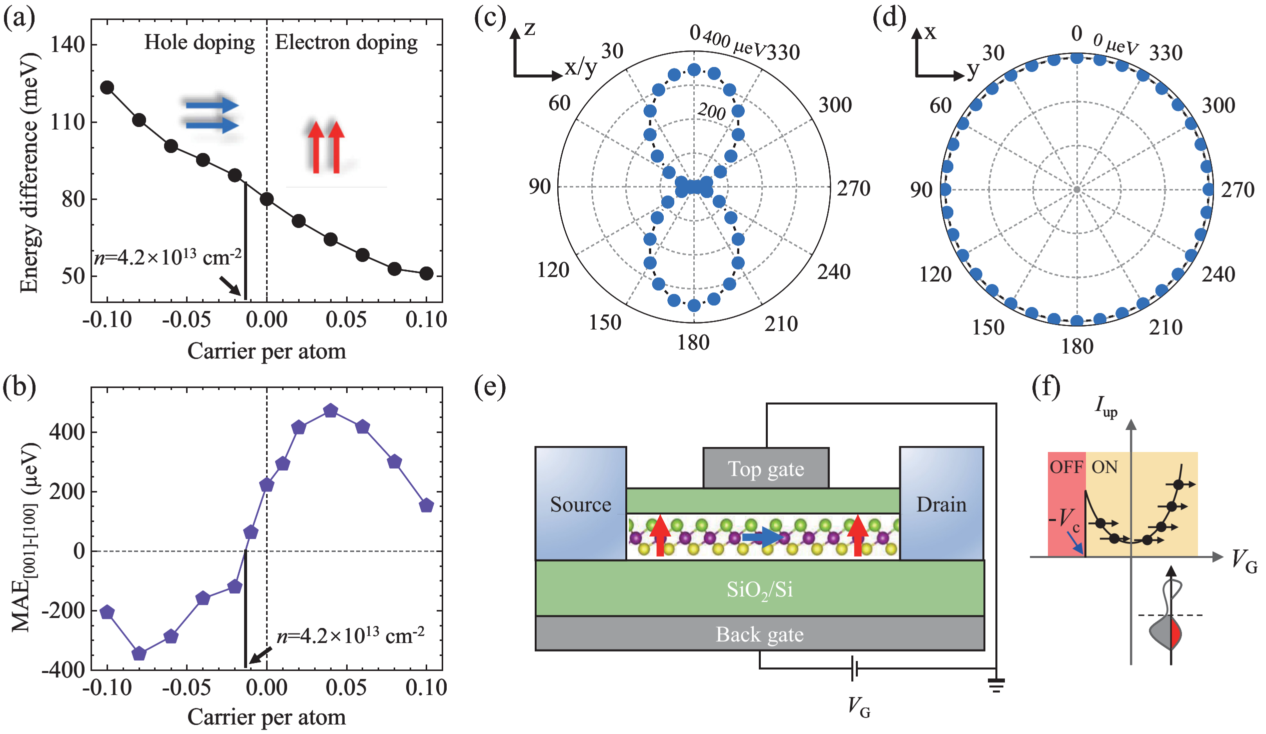

FIG. 4. (a) ΔE ($= E_{\mathrm{AFM}} - E_{\mathrm{FM}}$, in meV per unit cell) and (b) MAE $= E_{[001]} - E_{[100]}$ plotted as a function of carrier concentration up to $2.8 \times 10^{14}\,\mathrm{cm}^{-2}$ (0.1 electrons per atom). (c), (d) Dependence of the MAE on the out-of-plane polar angle θ and in-plane azimuth angle φ for MnSSe with carrier concentration of $n = 0.08$ holes per atom. (e) A schematic illustration of the proposed spin-FET with giant magnetoresistance effect based on the 2D MnSSe crystal. The gate voltage V_G is applied to control the carrier concentration and easy axis. (f) Schematic plot of the spin-down current I_{up} versus V_G, with $-V_c$ indicating the voltage that can introduce a concentration of n_c.

negative for the antiferromagnetic one. M_i and M_j are the spin magnetic moments of the nearest-neighbor unit cell. According to Fig. 2(a), the total energies per Mn for AFM and FM configurations can be written as (neglecting the MAE since it is relatively small)

$$E_{\mathrm{FM}} = \left(-\tfrac{1}{2} \times 6\right) JM^2 + E_0, \tag{5}$$

$$E_{\mathrm{AFM}} = \left(-\tfrac{1}{2} \times 2 + \tfrac{1}{2} \times 4\right) JM^2 + E_0, \tag{6}$$

where E_0 is the total energy excluding the magnetic coupling. The factor of $\frac{1}{2}$ is included because the nearest Mn-Mn interaction is shared between two adjacent unit cells. Therefore, the exchange coupling constant is straightforwardly calculated from $\Delta E = E_{\mathrm{AFM}} - E_{\mathrm{FM}} = 80\,\mathrm{meV}$ and $M = 3.0\mu_B$ with $J = (E_{\mathrm{AFM}} - E_{\mathrm{FM}})/(4JM^2)$, which is 2.22 meV. The estimated T_c is $\sim$194 K [Fig. 3(c)], very close to the previous report (185 K) [14], and dramatically larger than the recent experimental reports of 2D CrI$_3$ (45 K) [41,42] and Cr$_2$Ge$_2$Te$_6$ (20 K) [43].

The microscopic origin of FM coupling in MnSSe can be understood by the competition of direct exchange interaction (Mn-Mn) and the superexchange interaction (Mn-X-Mn, X = S or Se) mediated by the neighboring S and Se atoms, as shown in Fig. 3(d). For the direct interaction between the nearest-neighbor Mn, their d orbitals overlap directly, which gives rise to AFM coupling. The Goodenough-Kanamori-Anderson (GKA) rule proposes that FM coupling in systems with 90° bond angles is energy favorable. According to Launay and Wagner the exchange integral J in 2D materials has the approximate form of $J \approx 2k + 4\beta S$ [44]. The first term k is called the potential exchange, which is positive due to Hund's first rule [45]. The second term consists of the hopping integral β and overlap integral S. Since the bond angles of Mn-S-Mn (94.8°) and Mn-Se-Mn (88.7°) are very close to 90°, the Mn-d orbitals are therefore nearly orthogonal to the p orbitals of S and Se, leading to a negligible overlap integral [Fig. 3(e)], and hence a positive $J \approx 2k$. As such, 2D MnSSe nanosheet adopts a ferromagnetic ordering because of the relatively large FM superexchange interaction.

C. Carrier doping controlled magnetization transition

Recently, Jiang *et al.* demonstrated the controllability of the magnetic properties of 2D CrI$_3$ crystal by electrostatic doping, and observed an electron carrier doping induced AFM-FM transition [46]. The modulation of the easy magnetization axis of Fe monolayer adsorbed on graphene substrate by charge injection was theoretically proposed [47]. A transition from metal to half metal was also proposed in ScCl exfoliated nanosheet with hole doping [48]. We considered carrier concentration up to $2.4 \times 10^{14}\,\mathrm{cm}^{-1}$ (0.1 electrons/holes per atom).

Figure 4(a) displays the ΔE as a function of carrier concentration. Clearly, ΔE substantially increases (decreases) linearly with doping, demonstrating that the exchange coupling can be efficiently enhanced or quenched with carrier doping. Meanwhile, the FM state is always the ground state over the whole doping range, implying that the interaction between moments has maintained the FM state. This pronounced magnetic response toward carrier concentration could be attributed to the relatively enhanced through-space interactions and weakened through-bound interaction induced by carrier doping, since the crystal structure of MnSSe remains unchanged. The rapid and linear variation of magnetic response with carrier concentration in MnSSe monolayer can be used to design magnetoelectric coupling spintronics devices.

On the other hand, carrier doping changes not only the strength of magnetic coupling, but also MAE. Plotted in Fig. 4(b) is the total energy difference MAE $= E_{[001]} - E_{[100]}$ over a wide range of carrier concentrations. With electron charge doping, 2D MnSSe retains its out-of-plane easy axis nature. In contrast, the sign of MAE is changed from positive to negative when a small amount of hole charge is injected, implying a possible change in the easy magnetization situation. To characterize this change more visibly, as an example, we illustrated in Figs. 4(c) and 4(d) the MAEs of xz, yz, and xy planes for hole-doped MnSSe. Obviously, MAE is rather strongly dependent on the out-of-plane angle θ, and an easy xy plane is observed. Following the XY model [49], the critical temperature of the BKT transition can be calculated as

$$T_{\mathrm{BKT}} = \frac{0.89J}{k_B}, \tag{7}$$

where k_{B} is the Boltzmann constant, and $J = \Delta E/8$ [50–52]. For example, for the case of hole doping concentration at $n = 2.23 \times 10^{14}\ \mathrm{cm}^{-2}$ (0.08 holes per atom), we obtained $J =$ 13.9 meV, and the corresponding transition temperature T_{BKT} of 145 K, which is significantly higher than the liquid nitrogen temperature (77 K). For instance, the BKT transition has already been observed or predicted in many other systems, including 2D magnetic crystal [51–54], surface reconstructions [55], interface superconductors [56,57], and trapped atomic gas [58].

As discussed above, an unusual finding of electrically switchable transition between a low-temperature quasi-long-range ordered phase and a long-range ferromagnetic ordered one is constructed, in clear contrast to the relatively small changes of magnetic coupling strength and MAE predicated in other systems [41,59–61].

D. Spin-FET with giant magnetoresistance effect

The field-controllable spin-dependent transport is promising for spintronics. As to the applications, the doping-induced switch between the in-plane and out-of-plane directions of the easy axis can be used to design 2D magnetoelectric devices. As shown in Fig. 4(b), MnSSe is transformed from an out-of-plane ferromagnet to an in-plane one at hole doping with concentration above $n_{\mathrm{c}} = 4.2 \times 10^{13}\ \mathrm{cm}^{-2}$, as suggested by the reversible easy axis. In this case, the heteromagnetic interface that composes these two states appears around this critical point. The strong interface scattering will lead to a sharp decrease in conductivity or an insulator transition. Below critical doping, in contrast, MnSSe hosts low resistance. Based on the above description and discussion, 2D MnSSe nanosheet was proposed to construct spin FET with giant magnetoresistance effect. The device is schematically shown in Fig. 4(e). In short, MnSSe monolayer is double gated and directly sandwiched by top and bottom dielectric layers, e.g., SiO$_2$/Si. The gate voltage V_{G} is applied to control the carrier concentration and hence the easy axis. The source-drain voltage drives spin-polarized current.

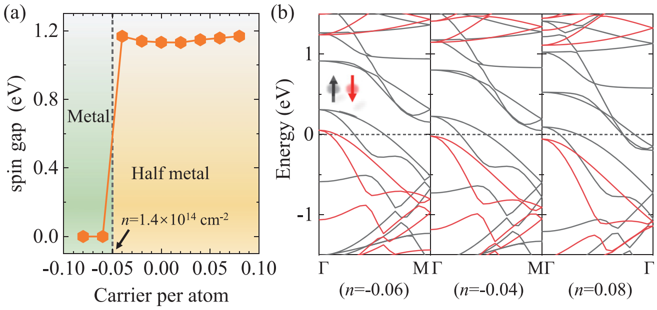

FIG. 5. (a) Variation of the band gap of spin-down channel with charge carrier concentration. (b) Three typical spin-polarized band structures.

One of the immediate consequences of injecting charge carrier in a crystal is the change of Fermi energy level. Figure 5(a) displays the variation of the band gap under carrier doping. As expected, MnSSe shows a transition to a ferromagnetic metal with moderate hole doping $n = 1.4 \times 10^{14}\ \mathrm{cm}^{-2}$ (0.5 holes per atom). Below this critical point, both carrier charge concentration and doping type have almost no effect on the size of the spin-gap [Fig. 5(b)], demonstrating the quite robust half-metallic ferromagnetism. Note that the critical doping for ferromagnetic metal is smaller than n_{c}, therefore the proposed device could conduct a 100% spin-up current I_{up}. Due to the doping effect, the carrier charge concentration can be controlled towards or away from the n_{c} by applied fields (voltages). The vertical electric field can act as a "gate" to switch the I_{up} [Fig. 4(f)], as such a spin FET operated purely via field is constructed. Although a room temperature device and double spin-polarized currents in MnSSe monolayer have not been achieved here, it is meaningful to note a rather strong magnetic coupling and bipolar control depending on crystal structure, constituent elements, and external interaction, etc. [62–65]. This leaves room for material selections. Previously, a modulation with charge density injected by using ionic liquid as gate dielectric at the level of $\sim 10^{15}\ \mathrm{cm}^{-2}$ has been reported in many 2D materials [66–68]. So, it is experimentally feasible to tune the magnetism by carrier doping and realize the 2D spin-FET proposed here.

E. Unique intralayer charge transfer

Carrier doping is mainly implemented by the liquid (or solid ionic) gating technique in experiments [69,70], where an external electric field is applied generally across the nanosheet. Therefore, it is necessary to find out the effect of this field on the physical properties of the material. As shown in Fig. 6(a), the field is applied parallel to the z axis, pointing from S to Se layer as indicated by the red arrow. The total energy of AFM and FM configurations with respect to $E_{\perp}$ is plotted in Fig. 6(b). The energy of the NM configuration

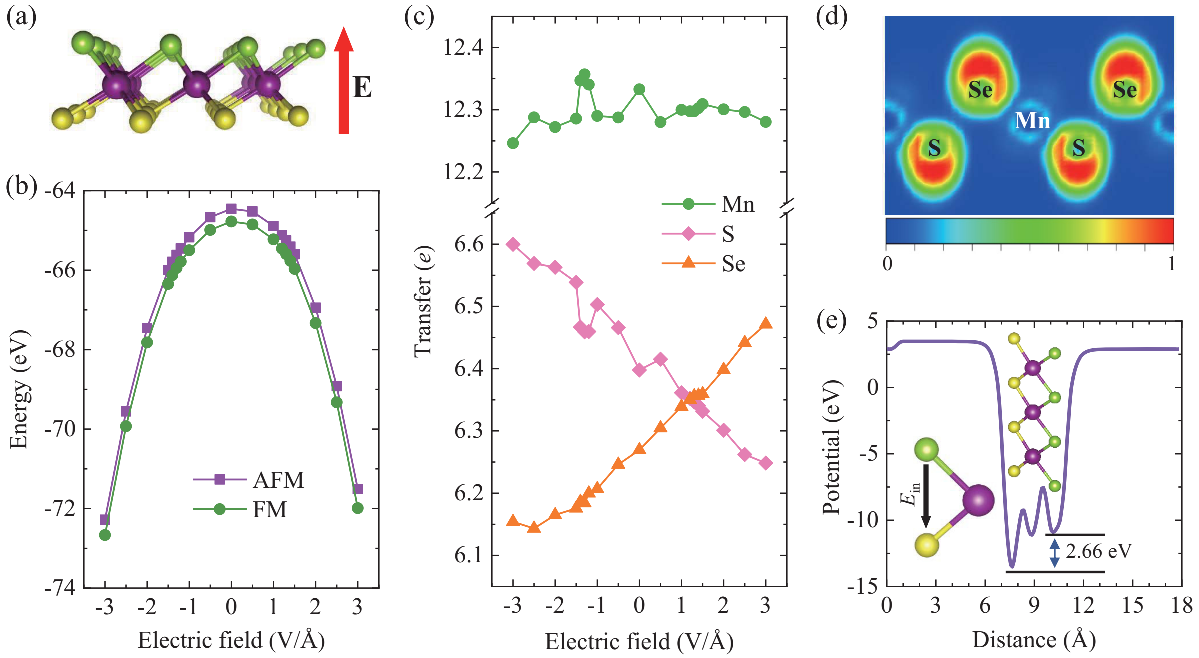

FIG. 6. (a) Scheme of the relation between MnSSe nanosheet and the applied external electric field $E_\perp$. The red arrow indicates the direction of both the positive electric field and the z axis. (c) System energies for AFM and FM configurations versus $E_\perp$, both with a dome shape. (c) Variation of the total charge of Mn, S, and Se atoms with respect to $E_\perp$. (d) ELF in (110) plane under zero filed. (e) Planar average of the electrostatic potential energy for MnSSe along the z direction under zero field. The inset shows the scheme of built-in electric field E_{in}.

is much higher than those of the magnetic ones, so it is not shown here. Both E_{AFM} and E_{FM} decrease in a quadratic way while the field increases away from zero, forming a domelike shape, implying that $E_\perp$ makes them more stable, in sharp contrast to the monotonically increased tendency theoretical reported in 2D nanosheet under strain [71,72]. The FM state always has lower energy than the AFM one, suggesting that the FM ordering is robust within a wide range of fields. Our test calculations also reveal that the crystal structure ΔE and band structure are minimally changed under a rather strong field. For instance, the influence of fields on crystal structure and energy has proved to be negligible [20,73].

Finally, we focused on the intralayer charge transfer behavior of Janus MnSSe monolayer. The Bader charge analysis shows that the electron number of both S and Se [S (N_{S}) and Se (N_{Se})] exhibit an approximately linear relation with external field in the range $E_\perp = -3$–$3\,\text{V/Å}$, while that of Mn (N_{Mn}) keeps mostly unchangeable [Fig. 6(c)]. This unique intralayer transfer constitutes the second major finding in this study. Moreover, N_{S} and N_{Se} varied reversely, implying that the charge transfer mainly occurs between S and Se atoms. What is far more important is that the electrons under external electric field are usually said to flow from the negative to the positive side of the field, which is opposite the observation here. As an example, when the field is applied from S to Se layer, i.e., the positive field we defined in Fig. 6(a), N_{S} decreases with increasing $E_\perp$; contrarily, N_{Se} increases with increasing $E_\perp$. To gain deeper insight into this anomalous behavior, we examine the bonding character by the electron localization function (ELF), which indicates the degree of electron localization. For clarity, the (110) plane cutting through two S atoms, two Se atoms, and two Mn atoms was selected and displayed in Fig. 6(d). Electrons are mainly localized around S and Se sites but rarely between S/Se and Mn atoms, suggesting the ionic character of Mn-S and Mn-Se bonds.

Due to the mirror asymmetry or electronegativity difference between S and Se atoms, N_{Se} is $0.2|e|$ less than N_{S} when $E_\perp = 0\,\text{V/Å}$, which may result in a built-in electric field, E_{in}. In support of this conjecture, we plot in Fig. 6(e) the planar averaged electrostatic potential energy along the z direction for MnSSe without external field. An intralayer potential gradient with a height of 2.66 eV is observed, indicating the existence of a net electric field pointing from Se to S layer. This indicates that this anomalous charge transfer is a joint effort of the external and the built-in electric fields. The increased $E_\perp$, with the positive field as a representative, weakens E_{in} and hence pushes electrons from S to Se. In addition, N_{S} departs from the linear relationship at $E_\perp = 0\,\text{V/Å}$ and $E_\perp = -1\,\text{V/Å}$, and manifests as two dips. Two peaks accordingly appear on the $N_{\text{Mn}}(E_\perp)$ curve at corresponding fields. Although in 2D crystals, cases about it are few, this unique behavior merits research.

IV. CONCLUSIONS

In summary, we have reported a promising alternative for tuning the magnetic coupling and electric structure in the monolayer MnSSe. We demonstrated that carrier doping can sensitively enhance or quench this ferromagnetic coupling.

The magnetization easy axis can be easily tuned between out of plane and in plane with a small amount of hole doping. These findings render MnSSe monolayer great potential for application in electrically controllable spintronic devices, such as spin FET with giant magnetoresistance effect. Also, a pronounced intralayer charge density response towards external electric field is reported, which is intriguing and could be considered as a new degree of freedom that will promote the development of nanoscale electronics and spintronics devices on the basis of 2D materials with asymmetrical structure.

ACKNOWLEDGMENTS

The authors thank Dr. J. He and H. Zhang for fruitful discussions. Part of this research used resources of Shanxi Supercomputing Center of China. This work was supported by the Scientific Research Project of Inner Mongolia University of Technology (Grant No. BS2021058), National Natural Science Foundation of China (Grant No. 12104294), and Research Program of Science and Technology at Universities of Inner Mongolia Autonomous Region (Grant No. NJZY22389).

[1] A. Fert, Rev. Mod. Phys. **80**, 1517 (2008).

[2] S. A. Wolf, D. D. Awschalom, R. A. Buhrman, J. M. Daughton, S. von Molnár, M. L. Roukes, A. Y. Chtchelkanova, and D. M. Treger, Science **294**, 1488 (2001).

[3] Q. H. Wang, K. Kalantar-Zadeh, A. Kis, J. N. Coleman, and M. S. Strano, Nat. Nanotechnol. **7**, 699 (2012).

[4] M. Gibertini, M. Koperski, A. F. Morpurgo, and K. S. Novoselov, Nat. Nanotechnol. **14**, 408 (2019).

[5] H. Yuan, M. S. Bahramy, K. Morimoto, S. Wu, K. Nomura, B.-J. Yang, H. Shimotani, R. Suzuki, M. Toh, C. Kloc *et al.*, Nat. Phys. **9**, 563 (2013).

[6] S. Wu, J. S. Ross, G.-B. Liu, G. Aivazian, A. Jones, Z. Fei, W. Zhu, D. Xiao, W. Yao, D. Cobden *et al.*, Nat. Phys. **9**, 149 (2013).

[7] Y. C. Cheng, Z. Y. Zhu, M. Tahir, and U. Schwingenschlögl, Europhys. Lett. **102**, 57001 (2013).

[8] A.-Y. Lu, H. Zhu, J. Xiao, C.-P. Chuu, Y. Han, M.-H. Chiu, C.-C. Cheng, C.-W. Yang, K.-H. Wei, Y. Yang *et al.*, Nat. Nanotechnol. **12**, 744 (2017).

[9] J. Zhang, S. Jia, I. Kholmanov, L. Dong, D. Er, W. Chen, H. Guo, Z. Jin, V. B. Shenoy, L. Shi *et al.*, ACS Nano **11**, 8192 (2017).

[10] X. Wang, D. Chen, Z. Yang, X. Zhang, C. Wang, J. Chen, X. Zhang, and M. Xue, Adv. Mater. **28**, 8645 (2016).

[11] M. L. Wenjun Liu, X. Liu, M. Lei, and Z. Wei, Opt. Lett. **45**, 419 (2020).

[12] Y. Guo, S. Zhou, Y. Bai, and J. Zhao, Appl. Phys. Lett. **110**, 163102 (2017).

[13] M. Yagmurcukardes, Y. Qin, S. Ozen, M. Sayyad, F. M. Peeters, S. Tongay, and H. Sahin, Appl. Phys. Rev. **7**, 011311 (2020).

[14] J. He and S. Li, Comput. Mater. Sci. **152**, 151 (2018).

[15] J. Wang, B. Lian, and S.-C. Zhang, Phys. Rev. Lett. **115**, 036805 (2015).

[16] T. M. R. Wolf, J. L. Lado, G. Blatter, and O. Zilberberg, Phys. Rev. Lett. **123**, 096802 (2019).

[17] H. Wang, J. Qi, and X. Qian, Appl. Phys. Lett. **117**, 083102 (2020).

[18] S. Jiang, J. Shan, and K. F. Mak, Nat. Mater. **17**, 406 (2018).

[19] Y. Y. Sun, L. Q. Zhu, Z. Li, W. Ju, S. J. Gong, J. Q. Wang, and J. H. Chu, J. Phys.: Condens. Matter. **31**, 205501 (2019).

[20] S. J. Gong, C. Gong, Y. Y. Sun, W. Y. Tong, C. G. Duan, J. H. Chu, and X. Zhang, Proc. Natl. Acad. Sci. U.S.A. **115**, 8511 (2018).

[21] M. Weisheit, S. Fähler, A. Marty, Y. Souche, C. Poinsignon, and D. Givord, Science **315**, 349 (2007).

[22] P. E. Blöchl, Phys. Rev. B **50**, 17953 (1994).

[23] G. Kresse and D. Joubert, Phys. Rev. B **59**, 1758 (1999).

[24] G. Kresse and J. Furthmüller, Phys. Rev. B **54**, 11169 (1996).

[25] J. P. Perdew, K. Burke, and M. Ernzerhof, Phys. Rev. Lett. **77**, 3865 (1996).

[26] S. L. Dudarev, G. A. Botton, S. Y. Savrasov, C. J. Humphreys, and A. P. Sutton, Phys. Rev. B **57**, 1505 (1998).

[27] J. He, P. Lyu, L. Z. Sun, Á. Morales García, and P. Nachtigall, J. Mater. Chem. C **4**, 6500 (2016).

[28] G. J. Ackland, M. C. Warren, and S. J. Clark, J. Phys.: Condens. Matter. **9**, 7861 (1997).

[29] A. Togo and I. Tanaka, Scr. Mater. **108**, 1 (2015).

[30] K. Momma and F. Izumi, J. Appl. Crystallogr. **44**, 1272 (2011).

[31] V. Wang, N. Xu, J.-C. Liu, G. Tang, and W.-T. Geng, Comput. Phys. Commun. **267**, 108033 (2021).

[32] L. M. Yang, I. A. Popov, T. Frauenheim, A. I. Boldyrev, T. Heine, V. Bacic, and E. Ganz, Phys. Chem. Chem. Phys. **17**, 26043 (2015).

[33] X. Li, X. Wu, and J. Yang, J. Am. Chem. Soc. **136**, 11065 (2014).

[34] X. Li and J. Yang, J. Mater. Chem. C **2**, 7071 (2014).

[35] J. Jiang, Q. Liang, R. Meng, Q. Yang, C. Tan, X. Sun, and X. Chen, Nanoscale **9**, 2992 (2017).

[36] F. Zheng, J. Zhao, Z. Liu, M. Li, M. Zhou, S. Zhang, and P. Zhang, Nanoscale **10**, 14298 (2018).

[37] A. Politano and G. Chiarello, Nano Res. **8**, 1847 (2015).

[38] T. J. Booth, P. Blake, R. R. Nair, D. Jiang, E. W. Hill, U. Bangert, A. Bleloch, M. Gass, K. S. Novoselov, M. I. Katsnelson *et al.*, Nano Lett. **8**, 2442 (2008).

[39] J. Yuan, Y. Yang, Y. Cai, Y. Wu, Y. Chen, X. Yan, and L. Shen, Phys. Rev. B **101**, 094420 (2020).

[40] J. M. Kosterlitz and D. J. Thouless, J. Phys. C: Solid State Phys. **6**, 1181 (1973).

[41] L. Webster and J.-A. Yan, Phys. Rev. B **98**, 144411 (2018).

[42] B. Huang, G. Clark, E. Navarro-Moratalla, D. R. Klein, R. Cheng, K. L. Seyler, D. Zhong, E. Schmidgall, M. A. McGuire, D. H. Cobden *et al.*, Nature (London) **546**, 270 (2017).

[43] C. Gong, L. Li, Z. Li, H. Ji, A. Stern, Y. Xia, T. Cao, W. Bao, C. Wang, Y. Wang *et al.*, Nature (London) **546**, 265 (2017).

[44] J.-P. Launay and M. Verdaguer, *Electrons in Molecules: From Basic Principles to Molecular Electronics,* 1st ed. (Oxford University Press, Oxford, 2013).

[45] P. A. Cox, *Transition Metal Oxides. An Introduction to their Electronic Structure and Properties* (Oxford University Press, Oxford, 2010).

[46] S. Jiang, L. Li, Z. Wang, K. F. Mak, and J. Shan, Nat. Nanotechnol. **13**, 549 (2018).

[47] S. J. Gong, C.-G. Duan, Z.-Q. Zhu, and J.-H. Chu, Appl. Phys. Lett. **100**, 122410 (2012).

[48] B. Wang, Q. Wu, Y. Zhang, Y. Guo, X. Zhang, Q. Zhou, S. Dong, and J. Wang, Nanoscale Horiz. **3**, 551 (2018).

[49] J. F. Fernández, M. F. Ferreira, and J. Stankiewicz, Phys. Rev. B **34**, 292 (1986).

[50] H. L. Zhuang and R. G. Hennig, Phys. Rev. B **93**, 054429 (2016).

[51] D. Dey and A. S. Botana, Phys. Rev. Mater. **4**, 074002 (2020).

[52] M. Ashton, D. Gluhovic, S. B. Sinnott, J. Guo, D. A. Stewart, and R. G. Hennig, Nano Lett. **17**, 5251 (2017).

[53] A. N. Ma, P. J. Wang, and C. W. Zhang, Nanoscale **12**, 5464 (2020).

[54] A. Bedoya-Pinto, J.-R. Ji, K. Pandeya Avanindra, P. Gargiani, M. Valvidares, P. Sessi, M. Taylor James, F. Radu, K. Chang, and S. P. Parkin Stuart, Science **374**, 616 (2021).

[55] D. H. Baek, J. W. Chung, and W. K. Han, Phys. Rev. B **47**, 8461 (1993).

[56] W. H. Zhang, Y. Sun, J. S. Zhang, F. S. Li, M. H. Guo, Y. F. Zhao, H. M. Zhang, J. P. Peng, Y. Xing, H. C. Wang *et al.*, Chin. Phys. Lett. **31**, 017401 (2014).

[57] N. Reyren, S. Thiel, A. D. Caviglia, L. F. Kourkoutis, G. Hammerl, C. Richter, C. W. Schneider, T. Kopp, A. S. Ruetschi, D. Jaccard *et al.*, Science **317**, 1196 (2007).

[58] Z. Hadzibabic, P. Krüger, M. Cheneau, B. Battelier, and J. Dalibard, Nature (London) **441**, 1118 (2006).

[59] Z. Guan and S. Ni, ACS Appl. Mater. Interfaces **12**, 53067 (2020).

[60] Q. Sun, S. Kwon, M. Stamenova, S. Sanvito, and N. Kioussis, Phys. Rev. B **101**, 134419 (2020).

[61] M. Abdollahi and M. Bagheri Tagani, J. Mater. Chem. C **8**, 13286 (2020).

[62] X. Li, X. Wu, Z. Li, J. Yang, and J. G. Hou, Nanoscale **4**, 5680 (2012).

[63] R. Chua, J. Zhou, X. Yu, W. Yu, J. Gou, R. Zhu, L. Zhang, M. Liu, M. B. H. Breese, W. Chen *et al.*, Adv. Mater. **33**, 2103360 (2021).

[64] S. Fu, K. Kang, K. Shayan, A. Yoshimura, S. Dadras, X. Wang, L. Zhang, S. Chen, N. Liu, A. Jindal *et al.*, Nat. Commun. **11**, 2034 (2020).

[65] C. Tang, K. K. Ostrikov, S. Sanvito, and A. Du, Nanoscale Horiz. **6**, 43 (2021).

[66] H. Yuan, H. Shimotani, A. Tsukazaki, A. Ohtomo, M. Kawasaki, and Y. Iwasa, Adv. Funct. Mater. **19**, 1046 (2009).

[67] A. S. Dhoot, C. Israel, X. Moya, N. D. Mathur, and R. H. Friend, Phys. Rev. Lett. **102**, 136402 (2009).

[68] J. T. Ye, S. Inoue, K. Kobayashi, Y. Kasahara, H. T. Yuan, H. Shimotani, and Y. Iwasa, Nat. Mater. **9**, 125 (2010).

[69] B. Lei, J. H. Cui, Z. J. Xiang, C. Shang, N. Z. Wang, G. J. Ye, X. G. Luo, T. Wu, Z. Sun, and X. H. Chen, Phys. Rev. Lett. **116**, 077002 (2016).

[70] T. P. Ying, M. X. Wang, X. X. Wu, Z. Y. Zhao, Z. Z. Zhang, B. Q. Song, Y. C. Li, B. Lei, Q. Li, Y. Yu *et al.*, Phys. Rev. Lett. **121**, 207003 (2018).

[71] Y. Ma, Y. Dai, M. Guo, C. Niu, Y. Zhu, and B. Huang, ACS Nano **6**, 1695 (2012).

[72] Y. Zhou, Z. Wang, P. Yang, X. Zu, L. Yang, X. Sun, and F. Gao, ACS Nano **6**, 9727 (2012).

[73] Q.-F. Yao, J. Cai, W.-Y. Tong, S.-J. Gong, J.-Q. Wang, X. Wan, C.-G. Duan, and J. H. Chu, Phys. Rev. B **95**, 165401 (2017).